Journal of MATERIALS RESEARCH

Invited Paper
DOI:10.1557/s43578-021-00375-3

ULTRA-WIDE BANDGAP MATERIALS, DEVICES, AND SYSTEMS

FOCUS ISSUE

Strain states and relaxation for α-$(Al_xGa_{1-x})_2O_3$ thin films on prismatic planes of α-Al_2O_3 in the full composition range: Fundamental difference of a- and m-epitaxial planes in the manifestation of shear strain and lattice tilt

Max Kneiß[1,a], Daniel Splith[1], Holger von Wenckstern[1], Michael Lorenz[1], Thorsten Schultz[2,3], Norbert Koch[2,3], Marius Grundmann[1]

[1] Universität Leipzig, Felix Bloch Institute for Solid State Physics, Semiconductor Physics Group, Linnéstraße 5, Leipzig 04103, Germany
[2] Humboldt Universität zu Berlin, Institut für Physik, Brook-Taylor-Straße 6, Berlin 12489, Germany
[3] Helmholtz-Zentrum für Energie und Materialien GmbH, Hahn-Meitner-Platz 1, Berlin 14109, Germany
[a] Address all correspondence to this author. e-mail: max.kneiss@physik.uni-leipzig.de

Received: 30 April 2021; accepted: 31 August 2021; published online: 22 September 2021

Pseudomorphic and relaxed α-$(Al_xGa_{1-x})_2O_3$ thin films are grown by combinatorial pulsed laser deposition in the entire composition range on prismatic a- and m-plane α-Al_2O_3 substrates. Pseudomorphic growth on m-plane sapphire has been achieved for $x \geq 0.45$. A distinct difference between the a- and m-epitaxial plane is observed in reciprocal space map measurements being in agreement with continuum elasticity theory for rhombohedral heterostructures. While pseudomorphic layers on m-plane sapphire show a pronounced shear strain e'_5 along the *c*-axis direction, relaxed layers exhibit a global lattice tilt in the same direction. Both effects are not present on the a-epitaxial plane. Out-of-plane lattice constants as well as e'_5 are modeled as function of *x* employing elasticity theory, confirming theoretical values of the elastic stiffness tensor for α-Ga_2O_3, especially the non-zero value of the C_{14} component. Possible pyramidal slip systems for strain relaxation in *c*-axis direction are examined to explain and numerically model the difference in lattice tilt for the two substrate orientations.

Introduction

Ga_2O_3 as wide bandgap semiconductor has received growing attention in the last two decades mainly due to the large predicted electric breakdown field of about 8 MV/cm for the thermodynamically stable monoclinic β-modification caused by its large bandgap of about 4.6 eV that allows for efficient power device applications [1]. Further, the growth of large single crystals from the melt is possible that triggered additional research efforts due to the possibility of homoepitaxial growth. Due to the limited electron mobility of the material, sophisticated heterostructure devices such as HEMTs based on β-$(Al_xGa_{1-x})_2O_3$/β-Ga_2O_3 heterointerfaces were utilized to localize two-dimensional electron gases (2DEGs) at the interface that increase the mobility [2–4]. This can be recapitulated in several recent reviews [1, 5–8]. However, lately, there is also increasing interest in the metastable modifications of Ga_2O_3, such as rhombohedral α-Ga_2O_3 in $R\bar{3}c$ corundum structure [9–11], orthorhombic κ-Ga_2O_3 [12, 13] or γ-Ga_2O_3 with defect spinel structure [14–16]. α-Ga_2O_3 possesses the largest bandgap of these polymorphs of about 5.3 eV [9] that would even further increase the expected breakdown voltage. Additionally, it can be grown heteroepitaxially with high quality on cost-effective isostructural α-Al_2O_3 substrates [17–22] (sapphire). It can be doped n-type utilizing, e.g., Si, Sn or F as dopants [22–26] and due to it being isostructural to α-Al_2O_3 the full compositional range of α-$(Al_xGa_{1-x})_2O_3$ from Ga_2O_3 to Al_2O_3 can be covered without miscibility gaps allowing bandgap engineering for HEMT structures or quantum wells from 5.3 eV to 8.8 eV [22, 27–33]. In most reports, α-Ga_2O_3 and α-$(Al_xGa_{1-x})_2O_3$ is grown on the basal c-plane of α-Al_2O_3 [9, 17–22, 24, 28, 29, 34, 35]. Lately, also the pyramidal r-plane [14, 31, 36–40] as well as the prismatic a- [14, 27, 32,

41, 42] and m-plane [26, 33, 42–44] of sapphire were utilized as epitaxial plane for the material. Especially the last one became interesting for potential device applications due to doped m-plane α-Ga_2O_3 exhibiting up to three times higher mobility than similar layers on c-plane sapphire [26]. Also, m-plane growth is beneficial for the stabilization of the α-phase due to the suppression of basal facets, where β-Ga_2O_3 favourably forms [33].

However, for the design and growth of heterostructure device applications and also the growth of the binary material, detailed knowledge about the strain distribution and relaxation processes of α-Ga_2O_3 and α-$(Al_xGa_{1-x})_2O_3$ is necessary. We recently reported on the heteroepitaxial stress and strain present in pulsed laser deposition (PLD) grown pseudomorphic r-plane α-$(Al_xGa_{1-x})_2O_3$/α-Al_2O_3 heterostructures that we modeled rigorously as well as with great accuracy based on our elasticity theory for rhombohedral heterostructures [31, 45, 46]. Further, also the relaxation processes for partially relaxed layers were understood and the prismatic a-planes identified as dominant slip system on the r-plane [31, 39]. The same elasticity theory was applied to reproduce the out-of-plane strain present in the pseudomorphic part of an α-$(Al_xGa_{1-x})_2O_3$ thin film with lateral composition gradient on a-plane sapphire grown by combinatorial PLD [32]. Crucial for the understanding of the heteroepitaxial strain is the knowledge about the entries of the elastic stiffness tensor C_{ij} in dependence on x. Up to now, for α-Ga_2O_3, they are exclusively available from theoretical calculations [47] as given later in this report. Due to the threefold pseudohexagonal rhombohedral $R\bar{3}c$ symmetry of the corundum structure, a distinct difference in biaxially strained α-$(Al_xGa_{1-x})_2O_3$/α-Al_2O_3 heterostructures for epitaxial a- and m-planes is expected [40, 45, 46]. This is caused by the nonvanishing C_{14} component of C_{ij} in contrast to "true" sixfold hexagonal systems such as wurtzite GaN or ZnO [48]. This should manifest itself in a shear strain present for heterostructures on the m-plane in contrast to the a-plane, if the theoretically calculated C_{14} component is correct. However, the epitaxial r-plane is relatively insensitive to the C_{14} component [31] and the m-plane α-$(Al_xGa_{1-x})_2O_3$ epilayers in literature were typically relaxed [33]. To the best knowledge of the authors, pseudomorphic growth on m-plane sapphire substrates was not yet reported. Additionally, a difference in strain relaxation for m-plane and a-plane epitaxial growth should be expected as well.

Here, we aim to understand the fundamental difference in the strain and relaxation of α-$(Al_xGa_{1-x})_2O_3$ epilayers on a- and m-plane sapphire as well as to confirm the theoretically calculated entries of the elastic stiffness tensor for α-Ga_2O_3. For this, we grew pseudomorphic as well as relaxed α-$(Al_xGa_{1-x})_2O_3$ thin films on m-plane as well as a-plane sapphire by combinatorial PLD employing only two radially-segmented targets to cover the entire composition range from α-Ga_2O_3 to α-Al_2O_3 with narrow steps in chemical composition (Discrete compositional screening (DCS) PLD [49, 50]). We performed a detailed and rigorous X-ray diffraction (XRD) examination of our layers and will show pseudomorphic growth with high crystalline quality of the layers on m-plane sapphire for $x_{Al} \geq 0.45$. The in- and out-of-plane lattice constants and shear strains of all layers shall be determined and modeled based on our stress-strain theory for rhombohedral heterostructures [45, 46] and the theoretically calculated stiffness tensor of α-Ga_2O_3 that is tested for accuracy especially of the C_{14} component. Further, the possible slip systems for strain relaxation in the m- and a-plane epilayers will be determined and based on that the composition-dependent lattice tilt in c-axis direction, only present for relaxed m-plane epilayers, will be reproduced.

Results and discussion

We first present the different typical effects associated with the pseudomorphic and relaxed growth of α-$(Al_xGa_{1-x})_2O_3$ on m-plane and a-plane sapphire substrates that can be observed in reciprocal space map measurements (RSMs). Schematic depictions of these effects in reciprocal space and the corresponding distortions of the lattice in real space can be found in Fig. S1 of the supplementary material. After that, we evaluate these measurements quantitatively and compare the results to elasticity theory as well as possible relaxation mechanisms. All of our samples grew phase pure in the α-phase and adopted the orientation of the substrate as expected due to the identical crystal symmetry. XRD 2θ-ω scans of the samples can be found in Fig. S2 in the supplementary material.

RSM measurements for α-$(Al_xGa_{1-x})_2O_3$ on m-plane and a-plane sapphire

Pseudomorphic layers

At first, we explain the differences of the growth on m- and a-plane sapphire for typical pseudomorphically strained α-$(Al_xGa_{1-x})_2O_3$ layers.

Figure 1a shows the RSMs around the symmetric (30.0) and asymmetric (22.0), $(4\bar{2}.0)$, $(30.\bar{6})$ and (30.6) reflections for a sample with $x = 0.8$ on m-plane sapphire with a thickness of $\approx$ 200 nm. For the (22.0) and $(4\bar{2}.0)$ reflections without c-axis component, i.e. measured in an azimuth where the c-axis is perpendicular to the plane of incidence of the X-ray beam, we observe the typical behavior of a pseudomorphically strained layer in reciprocal space. The reflections of the thin film are aligned in $q_{\parallel}$ with those of the substrate corresponding to an adoption of the in-plane lattice constant of the substrate. Further, the $q_{\perp}$ values of these reflections are the same as the one of the symmetric (30.0) reflection measured in the same azimuth corresponding to the same out-of-plane

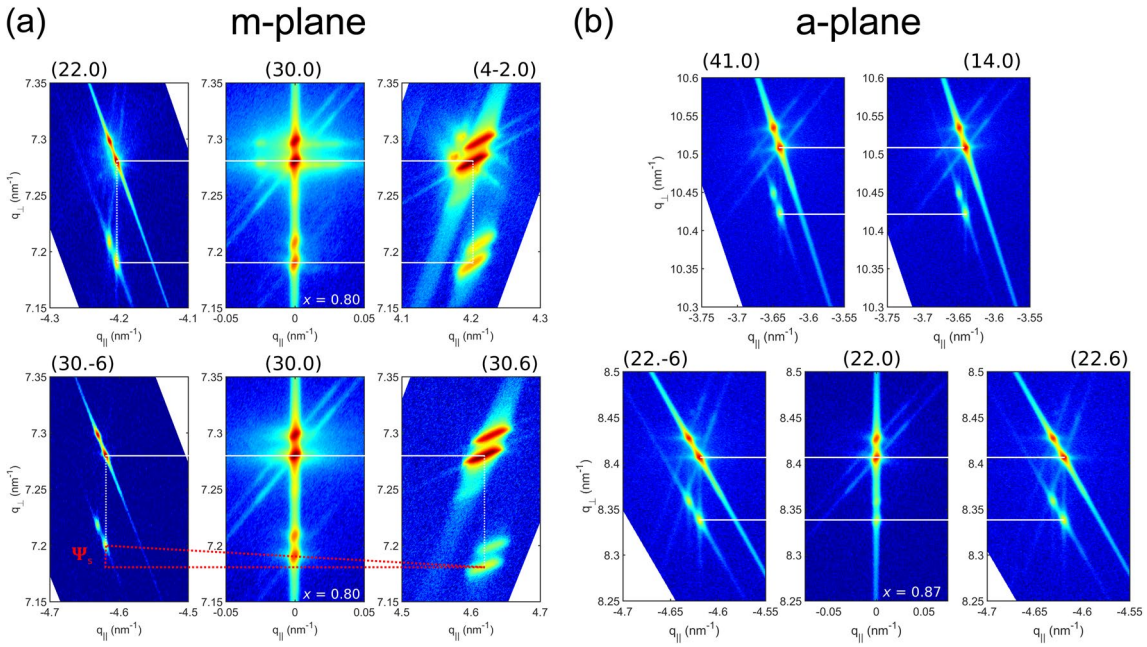

Figure 1: Typical RSMs for pseudomorphic α-$(Al_xGa_{1-x})_2O_3$ with Al-content x as indicated. The more intense reflections on top are always the reflections of the m- or a-plane α-Al_2O_3 substrate with distinct $K_{\alpha 1}/K_{\alpha 2}$ splitting and solid white lines are guides to the eye. (a) RSMs around the symmetric (30.0) and asymmetric (22.0), $(42\bar{.}0)$, $(30.\bar{6})$ and (30.6) reflections for a sample on m-plane sapphire. The two different (30.0) reflections were measured in the same azimuth as the asymmetric reflections in the upper or lower images, respectively. For the asymmetric reflections with a c-axis component in $q_\parallel$, a distinct difference between $q_\perp$ for positive and negative $q_\parallel$ positions of the reflections can be observed. This corresponds to a shear angle Ψ_s as indicated. (b) RSMs around the symmetric (22.0) and asymmetric (41.0), (14.0), $(22.\bar{6})$ and (22.6) reflections for a sample on a-plane sapphire. The (22.0) reflection was measured in the same azimuth as the asymmetric reflections in the lower images. The $q_\parallel$ values for all reflections are negative since they were all measured in grazing exit geometry and the sample was rotated by $\Delta\phi = 180°$ for the (22.6) and (14.0) reflection to decrease instrumental broadening that is enhanced for grazing incidence. In contrast to samples on m-plane substrates, no shear strain and corresponding shear angle can be observed.

component of the reflection. The reflections are very sharp and show a similar broadening as the ones of the substrate corroborating a high crystalline quality of the thin film layer.

For the $(30.\bar{6})$ and (30.6) reflections, however, we observe something different. While the reflections are still aligned with the substrate reflections in $q_\parallel$, they are shifted in the out-of-plane coordinates $q_\perp$ with respect to the symmetric (30.0) reflection in the same azimuth, one to lower and the other one to higher values. This is a consequence of a shear strain present in the thin film layer, i.e. the lattice is sheared in c-axis direction due to the pseudomorphic strain by a shear angle Ψ_s as predicted in Ref. [45]. The shear strain results in a rotation of the asymmetric reflections in reciprocal space by Ψ_s around the symmetric (30.0) reflection [51–53] as indicated in Fig. 1a. Since Ψ_s is typically very small, the difference in $q_\parallel$ due to the rotation is not noticeable in the RSM.

In contrast, for layers grown on a-plane sapphire, we could not observe shear strain for any sample we investigated as expected [45]. Fig. 1b shows typical RSMs around the symmetric (22.0) and asymmetric (41.0), (14.0), $(22.\bar{6})$ and (22.6) reflections of a sample on a-plane sapphire with $x = 0.87$. Neither in c-axis direction for the (22.6) and $(22.\bar{6})$ reflections nor perpendicular to it for the (41.0) and (14.0) reflection, we found any difference in the $q_\perp$ component for the samples. The RSMs in Fig. 1b were also all measured in grazing exit geometry to decrease the instrumental broadening of the reflections to ensure that also small effects are not overlooked.

Pseudomorphic growth of the samples with $\approx$ 200 nm thickness was only possible for $x \gtrsim 0.8$. For lower x, the critical thickness for coherent growth was exceeded and the thin films are partially or fully relaxed. For verification, we estimated a critical thickness of at least 220 nm for $x \approx 0.8$ on m-plane sapphire and at least 250 nm for $x \approx 0.86$ on a-plane sapphire, see Fig. S3 in the supplementary material. To further investigate and increase the strain effects that are enhanced for lower x, we successively decreased the layer thickness down to 30 nm, 20 nm and 10 nm for which we obtained pseudomorphic growth for Al-contents on m-plane sapphire as low as $x \approx 0.6$, $x \approx 0.55$ and $x \approx 0.45$, respectively. To the best knowledge of the authors, this is the lowest Al-content for which pseudomorphic growth has been observed, apart from three monolayer thick pseudomorphically strained binary α-Ga_2O_3 at the interface to the c-plane α-Al_2O_3

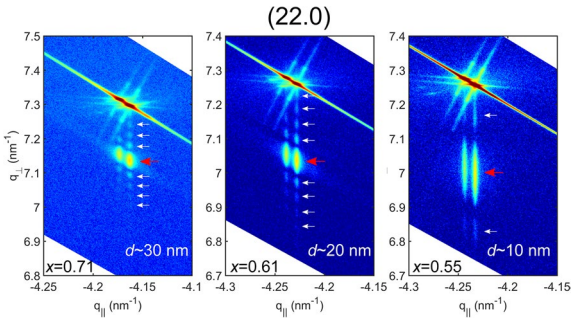

Figure 2: Typical RSMs around the asymmetric (22.0) reflections of thin pseudomorphic m-plane α-$(Al_xGa_{1-x})_2O_3$ samples with Al-contents x and thicknesses d as indicated. The more itense reflections on top are always the reflections of the m-plane α-Al_2O_3 substrate with distinct $K_{\alpha 1}$ /$K_{\alpha 2}$ splitting. The red arrow denotes the position of the $K_{\alpha 1}$ reflection of the α-$(Al_xGa_{1-x})_2O_3$ thin film while white arrows denote pronounced Pendellösung fringes that were also used to estimate the thickness of the samples and corroborate a high crystalline quality as well as smooth interfaces.

substrate of β-Ga_2O_3 layers [54] or 1 nm pseudomorphic α-Ga_2O_3 on a-plane α-Al_2O_3 [41].

Figure 2 shows typical RSMs around the asymmetric (22.0) reflection for three layers with different thickness as well as different values of x. Even the 10 nm samples exhibit sufficient intensity to clearly resolve the thin film reflections from the background. The red arrows mark the corresponding thin film reflections that become broader in the $q_\perp$ direction with decreasing thickness, but still exhibit the same broadening in $q_\parallel$ as the substrate reflections. Further, we can typically observe pronounced Pendellösung fringes close to the layer reflections up to the fourth order (white arrows). The separation of the fringes decreases with increasing film thickness in accordance to the expected behavior. From the separation of the fringes, the thickness of the layers was estimated. The 200 nm samples exhibit hints for Pendellösung fringes as well, however, they are too narrowly spaced for the reflections we measured and often rather appear as streak, see for example the $(22.\bar{6})$ reflection in Fig. 1b.

The occurrence of the Pendellösung fringes and the low broadening in $q_\parallel$ further confirm the excellent crystalline quality of our layers as well as smooth interfaces. The increase in broadening in $q_\perp$ agrees with the expected broadening due to the limited film thickness and is no sign of inferior crystalline quality.

Relaxed layers

When strain relaxation sets in, we typically can observe various effects that are also occurring differently for m-plane and a-plane sapphire substrates.

Figure 3a shows the RSMs around the symmetric (30.0) and asymmetric (22.0), $(4\bar{2}.0)$, $(30.\bar{6})$ and (30.6) reflections typical for a relaxed sample with $x = 0.04$ on m-plane sapphire. For the reflections without c-axis component, we see the behavior that is expected for a relaxed thin film layer. Reflections of the relaxed layers show generally a much larger broadening compared to the pseudomorphic layers. The (22.0) and $(4\bar{2}.0)$ reflections are shifted to lower positions both in $q_\perp$ and $q_\parallel$ due to the lattice expansion when the larger Ga atoms are introduced. The $q_\perp$ components are here also aligned with the one of the symmetric (30.0) reflection, which is located at $q_\parallel = 0$.

This is different for the reflections with c-axis component and also the symmetric (30.0) reflection in the same azimuth. Apparent is the shift of the symmetric reflection from $q_\parallel = 0$. The reciprocal lattice in this direction is rotated by an angle θ_T with respect to the origin of reciprocal space as indicated in Fig. 3a. This corresponds to a global tilt of the epitaxial plane of the thin film lattice with respect to the one of the substrate by θ_T along the c-axis caused by the relaxation mechanism that prevails.

This is not the case for the samples on a-plane sapphire. Fig. 3b shows the symmetric (22.0) reflections of several relaxed layers on a-plane sapphire with different values of x. The reflections were recorded both in an azimuth where the c-axis lies within the plane of incidence as well as perpendicular to it, i.e. the sample was rotated by $\Delta\phi = 90°$. For all samples and azimuths, the symmetric reflections are located at $q_\parallel = 0$ corresponding to negligible lattice tilt.

Quantitative evaluation of RSM measurements and comparison to elasticity theory

To obtain correct values for the lattice constants, several corrections need to be applied to the RSM data. First, sample tilt and goniometer errors need to be corrected by a comparison of the measured and theoretical positions of the substrate reflections. The difference is corrected by a transformation of the coordinate system of the RSM such that the substrate reflections are at the correct positions. Afterwards, the tilt angle can be determined from the position of the symmetric thin film reflections via

$$\cos\theta_T = \frac{q_{\perp,\mathrm{symm}}}{\sqrt{q^2_{\perp,\mathrm{symm}} + q^2_{\parallel,\mathrm{symm}}}} \quad (1)$$

After a rotation of the thin film reflections by θ_T around the center of the coordinate system, the shear angle can be determined from a pair of asymmetric reflections with nominally identical magnitudes of the positions in reciprocal space, but opposite signs of $q_\parallel$, e.g. $(30.\bar{6})$ and (30.6), via

$$\tan\Psi_s = \frac{q_{\perp,+} - q_{\perp,-}}{q_{\parallel,+} - q_{\parallel,-}} \quad (2)$$

Finally, the asymmetric reflections are rotated around the position of their corresponding symmetric reflection, e.g. (30.0)

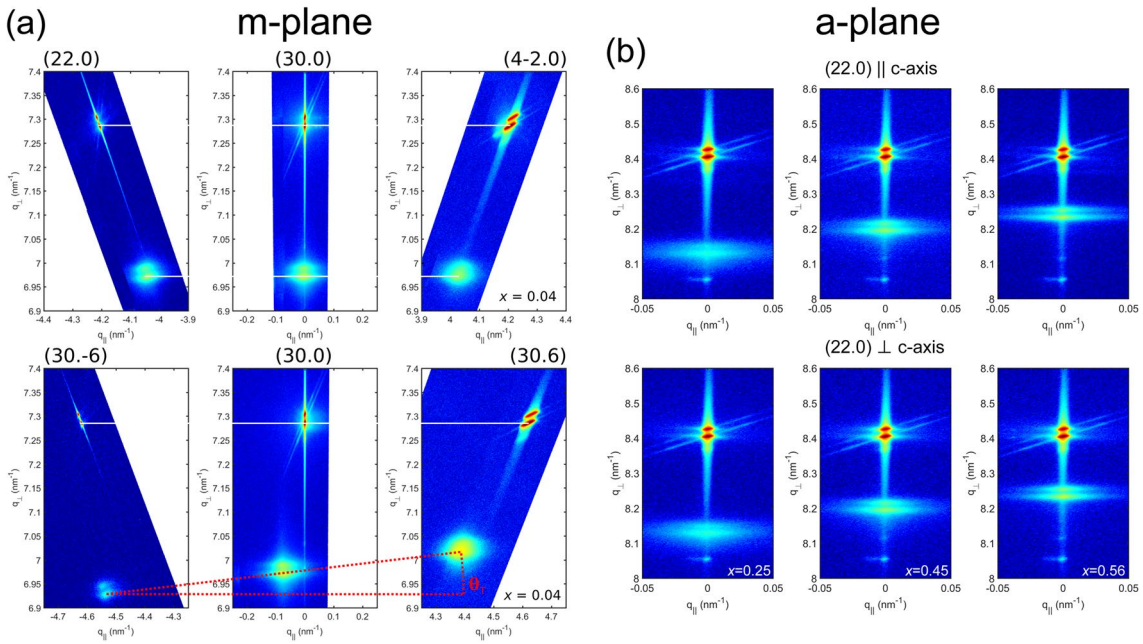

Figure 3: Typical RSMs of relaxed α-$(Al_xGa_{1-x})_2O_3$ epilayers with Al-content x as indicated. The more intense reflections on top are always the reflections of the m- or a-plane α-Al_2O_3 substrate with distinct $K_{\alpha 1}/K_{\alpha 2}$ splitting and solid white lines are guides to the eye. (a) RSMs around the symmetric (30.0) and asymmetric (22.0), (4$\bar{2}$.0), (30.$\bar{6}$) and (30.6) reflections for a sample on m-plane sapphire. The two different (30.0) reflections were measured in the same azimuth as the asymmetric reflections in the upper or lower images, respectively. For the asymmetric reflections with a c-axis component in $q_{||}$, a distinct tilt of the reciprocal lattice can be observed. This corresponds to a tilt angle θ_T as indicated. Solid white lines are guides to the eye. (b) RSMs around the symmetric (22.0) reflections for samples with different x on a-plane sapphire. The (22.0) reflections on top were measured in an azimuth with the c-axis within the plane of incidence of the X-ray beam, while the corresponding ones on the bottom were measured at $\Delta\phi = 90°$, i.e. in an azimuth where the c-axis was perpendicular to the plane of incidence. In contrast to the layers on m-plane sapphire, no tilt of the reciprocal lattice points was observed for any sample.

for (30.6), by Ψ_s. From the corrected positions in reciprocal space, the lattice constants can be calculated. For all reflections, the same lattice parameters were obtained after the correction within the experimental error, which served as self consistency check for the procedure. To further increase the accuracy, all reflections for the pseudomorphic samples were measured in grazing exit geometry, which decreases the instrumental broadening of the reflections. This is increased in grazing incidence geometry as for example given in Fig. 1a for the (4$\bar{2}$.0) and (30.6) reflections in contrast to the (22.0) and (30.$\bar{6}$) reflections that were measured in grazing exit geometry.

In reports on α-$(Al_xGa_{1-x})_2O_3$ layers on m-plane sapphire, only one asymmetric reflection is typically evaluated to determine strain state and lattice constants of the epilayer [33]. However, one should be aware that for an accurate determination of those properties, the measurement of several reflections is necessary to obtain correct results due to the aforementioned effects on this epitaxial plane.

Figure 4 shows the out-of-plane a-lattice constants as well as the in-plane a- and c-lattice constants for all investigated samples as function of x. The obtained shear angles are summarized in Fig. 5a and the tilt angles are depicted in Fig. 8a for all samples on m-plane sapphire as function of x as well. Note that in the case of the out-of-plane a-lattice constant for the m-plane samples as well as for the in-plane a-lattice constant of the a-plane samples, we calculated the associated a-lattice constant from the lattice plane distance $d_{10.0}$ of the corresponding {10.0} plane extracted from the RSMs via $a = \frac{2\sqrt{3}}{3} d_{10.0}$. Strictly, there is no well-defined a-lattice constant in these cases, since for these directions, no crystallographic a-plane with the corresponding lattice plane distance as a rational fraction of the a-lattice constant is existing, i.e. no a_i-axis vector is pointing in these directions, see also the unit cell orientations as schematically depicted in Fig. 7. All values shown here are given as a-lattice constants for comparison to highlight the similarities of a- and m-epitaxial planes regarding the fully-strained and relaxed lattice constants.

The out-of-plane a-lattice constants as well as the in-plane c-lattice constants of the relaxed samples closely follow the theoretical evolution of the bulk lattice constants $a_F(x)$ and $c_F(x)$ as expected from Vegard's law (black dashed lines), which should be a linear function of x.

The utilized lattice parameters of the binary materials are given in Table 1. The in-plane a-lattice constants of the relaxed samples, however, are slightly lower than expected. This might correspond to a low residual compressive in-plane strain in the a-axis direction. A corresponding low tensile strain might be

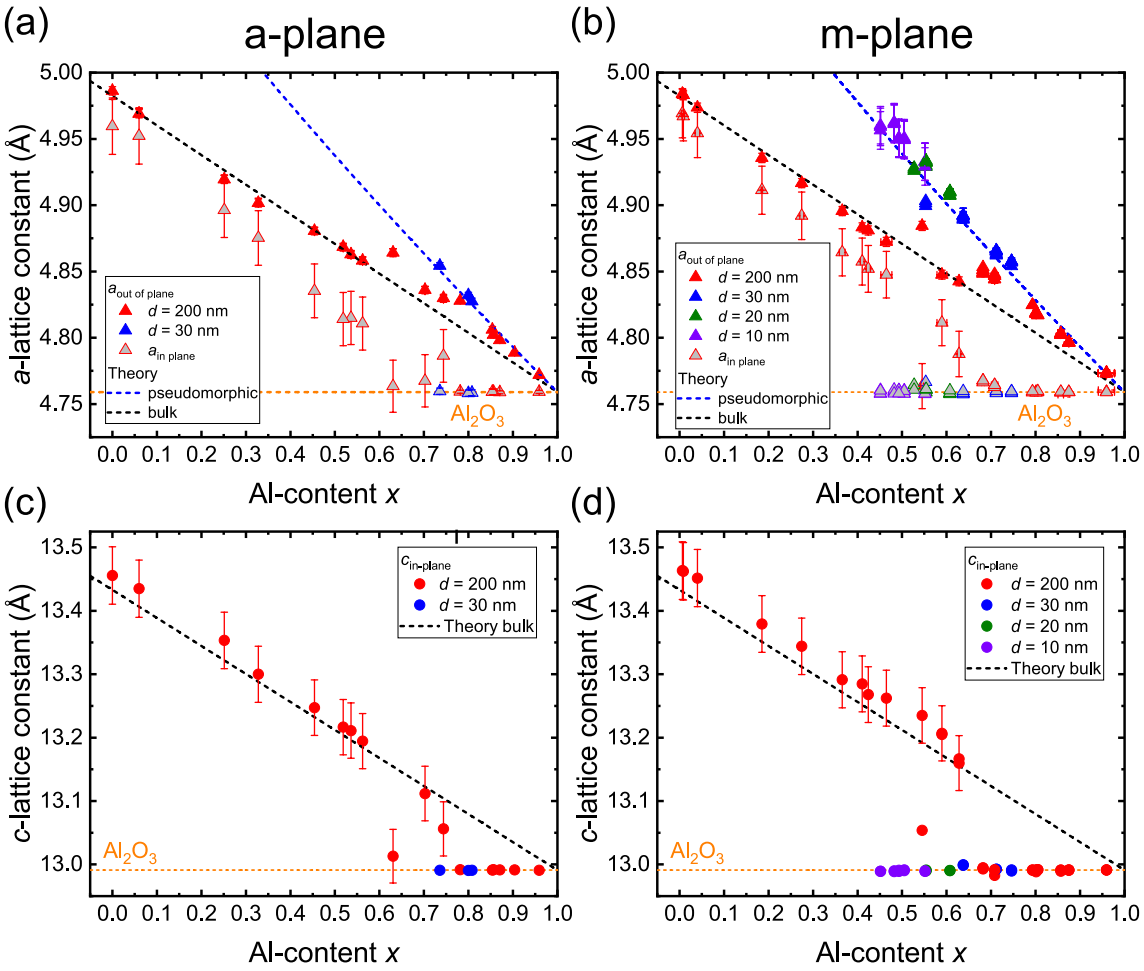

Figure 4: In- and out-of-plane lattice constants of all α-$(Al_xGa_{1-x})_2O_3$ samples as obtained from the evaluation of the RSM measurements as explained in the text. Triangular and circular symbols correspond to experimental values, while dashed lines are theoretically calculated curves in all panels. The approximate sample thickness *d* is color coded as given in the legends. The same color code applies for the completely colored symbols and the symbols with grey filling. (a) and (b) depicts the in- and out-of-plane *a*-lattice constants of all samples as function of the Al-content *x* for samples (a) on a-plane sapphire and (b) on m-plane sapphire, respectively. The blue dashed line corresponds to the out-of-plane *a*-lattice constant for pseudomorphic thin films as expected from elasticity theory given in Eqs. 6 and 10 for a-plane and m-plane orientation, respectively. (c) and (d) in-plane *c*-lattice constant of samples on (c) a-plane sapphire and (d) m-plane sapphire. The black dashed lines for all panels is the bulk lattice constant for relaxed samples as expected from Vegard's law. The orange dashed lines are the lattice constants of the α-Al_2O_3 substrate.

interpreted into the *c*-lattice data and also a residual shear strain different from zero within the experimental error in the *c*-axis direction for the relaxed samples on m-plane sapphire as given in Fig. 5a could be a consequence of the insufficient strain relaxation in *a*-axis direction. Another possible explanation could be additional asymmetric thermal strain as consequence of the different and anisotropic thermal expansion coefficients of α-Al_2O_3 and α-Ga_2O_3 in *a*-axis and *c*-axis direction [55–57]. Also, while the *c*-axis component of the thermal expansion coefficient of α-Ga_2O_3 is always about 25% larger than the one of α-Al_2O_3 from room temperature to about 700°C, the difference in the thermal expansion coefficient in *a*-axis direction changes sign at about 200°C [55–57]. Below this temperature, the value for α-Ga_2O_3 becomes lower than for α-Al_2O_3 that might result in a total compressive strain in *a*-axis and tensile strain in *c*-axis direction. However, additional experimental error for the in-plane coordinate could be possible as well since the reflections of the relaxed samples show increased broadening in $q_{\|}$ that also affects the correction procedure for the tilt angle not included in the error bars in Fig. 4. Additional microcrystalline methods such as transmission electron microscopy investigations are necessary to resolve this issue, which are not in the scope of this report.

The pseudomorphically strained samples all necessarily exhibit the in-plane lattice constants of the α-Al_2O_3 substrate and a vanishing tilt angle. The out-of-plane *a*-lattice constants are increased compared to the bulk value and the shear angle in *c*-axis direction for the m-plane samples is significantly

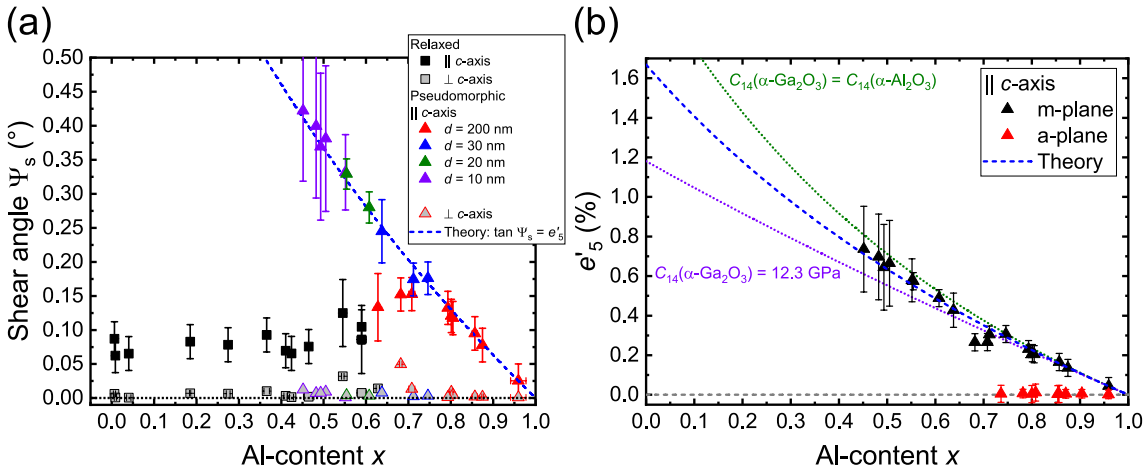

Figure 5: (a) Shear angle Ψ_s calculated from the RSM measurements for the samples on m-plane sapphire as function of Al-content x for an azimuth with the c-axis within the plane of incidence of the X-ray beam (|| c-axis) as well as perpendicular to it (⊥ c-axis). Triangular and quadratic symbols correspond to the determined experimental values. The approximate sample thickness d is color coded as given in the legend. The same color code applies for the completely colored symbols and the symbols with grey filling. The relaxed samples all exhibit a thickness of nominally 200 nm. (b) Shear strain $e'_5 = \tan \Psi_s$ as function of Al-content x for samples on m-plane and a-plane sapphire as indicated. The grey dashed line is a guide to the eye at zero strain. The blue dashed line is the expected evolution of shear angle and shear strain e'_5 as given in Eq. 11. An excellent agreement with theory is found that confirms the validity and value of the C_{14} component for the stiffness tensor of α-Ga_2O_3 and α-Al_2O_3. The dotted lines are theoretical curves for different values of C_{14} for α-Ga_2O_3 as indicated for comparison.

TABLE 1: Elastic constants and hexagonal lattice parameters of rhombohedral ($R\bar{3}c$) Al_2O_3 and Ga_2O_3.

Material	C_{11}	C_{12}	C_{13}	C_{33}	C_{14}	C_{44}	a (Å)	c (Å)
α-Al_2O_3	4.97	1.63	1.16	5.01	0.22	1.47	4.759	12.991
α-Ga_2O_3	3.815	1.736	1.26	3.458	0.173	0.797	4.9825	13.433

Values of the elastic constants given in units of 10^{11} Pa. Values for Al_2O_3 taken from Refs. [58] and [59] and for Ga_2O_3 from Refs. [47] and [60].

different from zero due to the compressive in-plane strain imposed by the substrate.

We numerically modeled the out-of-plane lattice constants as well as the shear strains based on continuum elasticity theory as derived in Refs. [45] and [46]. The stress-strain relation in the crystal system for a rhombohedral system with $R\bar{3}c$ crystal symmetry reads

$$\begin{pmatrix}\sigma_1\\ \sigma_2\\ \sigma_3\\ \sigma_4\\ \sigma_5\\ \sigma_6\end{pmatrix} = \begin{pmatrix} C_{11} & C_{12} & C_{13} & C_{14} & 0 & 0\\ C_{12} & C_{11} & C_{13} & -C_{14} & 0 & 0\\ C_{13} & C_{13} & C_{33} & 0 & 0 & 0\\ C_{14} & -C_{14} & 0 & C_{44} & 0 & 0\\ 0 & 0 & 0 & 0 & C_{44} & C_{14}\\ 0 & 0 & 0 & 0 & C_{14} & C_{66}\end{pmatrix} \begin{pmatrix} e_1\\ e_2\\ e_3\\ e_4\\ e_5\\ e_6\end{pmatrix}, \quad (3)$$

where $C_{66} = (C_{11} - C_{12})/2$. We utilize Voigt notation for the stress-strain relation, i.e. the strains are given by $e_1 = \varepsilon_{xx}$, $e_2 = \varepsilon_{yy}, e_3 = \varepsilon_{zz}, e_4 = 2\varepsilon_{yz}, e_5 = 2\varepsilon_{xz}$ and $e_6 = 2\varepsilon_{xy}$, with symmetrized $\varepsilon_{ij} = \frac{1}{2}\left(\frac{\partial u_i}{\partial x_j} + \frac{\partial u_j}{\partial x_i}\right)$, and the stresses are correspondingly given by $\sigma_1 = \sigma_{xx}, \sigma_2 = \sigma_{yy}, \sigma_3 = \sigma_{zz}, \sigma_4 = \sigma_{yz}, \sigma_5 = \sigma_{xz}$, and $\sigma_6 = \sigma_{xy}$. The u_i are the displacements in the crystal. With this, the stiffness tensor C_{ijkl} can be reduced to the symmetrized 6×6 matrix C_{ij} given above as explained in detail in Ref. [45]. Note that for a hexagonal system, such as wurtzite GaN or ZnO, the C_{14} component is equal to zero.

A rotational transformation into the laboratory system for the different epitaxial planes, as explained in Refs. [45] and [46], the conditions $\sigma'_{zz} = \sigma'_{xz} = \sigma'_{yz} = 0$ for the stresses and the known strains e'_1, e'_2 and e'_6 in the laboratory system are then utilized to calculate the unknown strains e'_3, e'_4, and e'_5. This procedure delivers for the a-growth plane:

$$e'_1 = \varepsilon'_{xx} = \frac{c_s}{c_F} - 1 \quad (4)$$

$$e'_2 = \varepsilon'_{yy} = \frac{a_s}{a_F} - 1 \quad (5)$$

$$e'_3 = \varepsilon'_{zz} = -\frac{C_{13}e'_1 + C_{12}e'_2}{C_{11}} \quad (6)$$

$$e'_4 = e'_5 = e'_6 = 0\,, \quad (7)$$

where a_s and c_s are the lattice constants of the α-Al_2O_3 substrate. For the m-growth plane, we obtain

$$e'_1 = \varepsilon'_{xx} = \frac{c_s}{c_F} - 1 \tag{8}$$

$$e'_2 = \varepsilon'_{yy} = \frac{a_s}{a_F} - 1 \tag{9}$$

$$e'_3 = \varepsilon'_{zz} = -\frac{C_{13}\, C_{44}\, e'_1 + (C_{12}C_{44} + C_{14}^2)\, e'_2}{C_{11}C_{44} - C_{14}^2} \tag{10}$$

$$e'_5 = 2\varepsilon'_{xz} = \frac{C_{14}\,(C_{13}\, e'_1 + (C_{11} + C_{12})\, e'_2)}{C_{11}C_{44} - C_{14}^2} \tag{11}$$

$$e'_4 = e'_6 = 0\,. \tag{12}$$

The out-of-plane lattice constants can then be calculated from the out-of-plane strain ε'_{zz} in the laboratory system:

$$a_{out}(x_{Al}) = a_F(x_{Al})\left[1 + \varepsilon'_{zz}(x_{Al})\right]. \tag{13}$$

The shear angle Ψ_s can be connected to the shear strain components via the differential displacements in the lattice.

$$\varepsilon'_{xz} = \frac{1}{2}\left(\frac{\partial u'_x}{\partial z} + \frac{\partial u'_z}{\partial x}\right) = \frac{1}{2}\frac{\partial u'_x}{\partial z} \tag{14}$$

$$\Rightarrow \tan\Psi_s = \frac{\partial u'_x}{\partial z} = 2\varepsilon'_{xz} = e'_5\,. \tag{15}$$

Note, $\frac{\partial u'_z}{\partial x} = 0$ is due to the vanishing tilt angle for the pseudomorphic layers and is a consequence of the imposed biaxial strain and the coherent film-substrate interface.

The manifestation of a shear angle along the c-direction for the growth on the m-plane in contrast to growth on the a-plane is therefore a consequence of Eqs. 7 and 11, i.e. a non-vanishing e'_5 component only for the m-growth plane. This in turn is a direct consequence of the non-vanishing C_{14} component of the stiffness tensor in the rhombohedral $R\bar{3}c$ crystal symmetry. For $C_{14} = 0$, the exact same strain relations hold for a-plane and m-plane systems.

We have interpolated the elastic constants C_{ij} for α-Ga_2O_3 and α-Al_2O_3 linearly as given in Table 1 for the $C_{ij}(x)$ for α-$(Al_xGa_{1-x})_2O_3$ to calculate the relevant strains, lattice constants and shear angles for our pseudomorphic samples as function of x. Note that the sign of C_{14} of α-Ga_2O_3 in Ref. [47] is opposite to the one given here. This is solely due to the specific choice of the coordinate system [31] and C_{14} should not change sign for α-$(Al_xGa_{1-x})_2O_3$. The result is shown in Fig. 4 and 5 as blue dashed lines. The out-of-plane a-lattice constants follow the theoretical curve with very good agreement corroborating our previous studies for epilayers on r-plane [31] as well as on a-plane sapphire [32]. The curves for a- and m-growth planes are relatively similar due to the out-of-plane strain ε'_{zz} being quite insensitive to the C_{14} component in the case of m-plane sapphire, since C_{14}^2/C_{44} is small compared to C_{11}, C_{12} and C_{13} [31].

The shear strain e'_5 in Eq. 11, however, has a direct linear proportionality to the C_{14} component and is quite sensitive to its value. Using the linear interpolation of the experimental values of α-Al_2O_3 and the theoretical values for α-Ga_2O_3, we can reproduce the shear angle with high accuracy (blue dashed line in Fig. 5a and for a large range in x. Fig. 5b shows further the e'_5 component calculated from the shear angles in c-axis direction for pseudomorphic layers on m-plane and a-plane sapphire in comparison. e'_5 for the m-growth plane is clearly non-vanishing and in very good agreement with the theoretical curve. For comparison, curves with a variation of $C_{14}(\alpha$-$Ga_2O_3)$ are shown as well. The e'_5 component for the layers on a-plane sapphire in contrast is equal to zero over a broad range of x. A fit to the e'_5 data for the m-plane samples for $C_{14}(\alpha$-$Ga_2O_3)$ delivers a value of $C_{14}(\alpha$-$Ga_2O_3) = (17.9 \pm 1)$ GPa when the experimental errors are not included in the weighting of the fit. When the errors are included as instrumental weight, we obtain $C_{14}(\alpha$-$Ga_2O_3) = (15.8 \pm 1.7)$ GPa, both close to the value given in Table 1. This finding greatly corroborates the validity of the continuum elasticity theory approach as given in Refs. [45] and [46] and also validates the theoretical value of C_{14} for α-Ga_2O_3 reported in Ref. [47].

We further calculated the shear strain component e'_5 as function of the inclination angle θ_s of the epitaxial plane with respect to the c-plane in the r- (01.2) and r′-plane (10.2) azimuth for a pseudomorphically strained α-$(Al_{0.8}Ga_{0.2})_2O_3/\alpha$-$Al_2O_3$ heterostructure, both for the interpolated value of C_{14} for $x = 0.8$ as well as for $C_{14} = 0$ for comparison. The result is shown in Fig. 6. As one can clearly observe, the m-plane is actually the best suited plane to test the accuracy of the C_{14} component since the relative difference in e'_5 compared to a vanishing C_{14} component is the largest. The r- and r′-planes we investigated in previous studies in detail [31, 39, 40], however, show only little sensitivity of e'_5 to C_{14}, which is almost vanishing for the r-plane inclination angle in Fig. 6. This is the reason why no shear strain was detected in our previous reports on the growth on r-plane sapphire and further confirms the validity of the elasticity theory. In the final part of this report, we will shed light on the difference in relaxation and the manifestation of a tilt angle only for the m-growth plane.

Difference in layer relaxation

Possible slip systems for strain relaxation

Plastic strain relaxation is typically mediated by misfit dislocations at the heterostructure interface. The dislocations can move

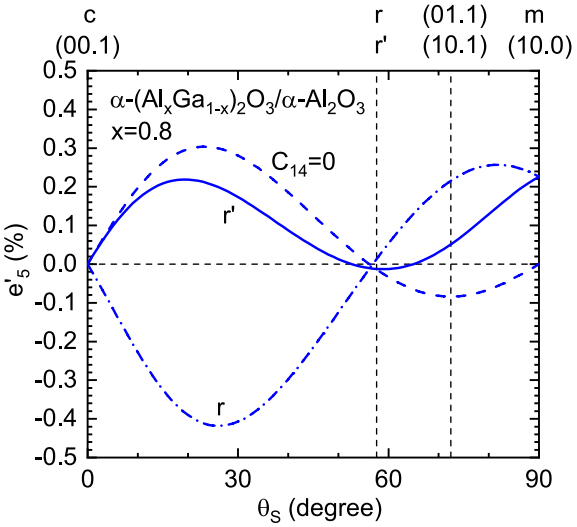

Figure 6: Expected value of the shear strain e'_5 for a pseudomorphically strained α-$(Al_{0.8}Ga_{0.2})_2O_3/\alpha$-$Al_2O_3$ heterostructure as function of the inclination angle θ_s of the growth plane in the azimuth of r and r′-plane as defined in Refs. [45] and [31] for an interpolated $C_{14}(x = 0.8) = 21.06$ GPa. The blue dashed line is the expected value for a vanishing C_{14} component for comparison that is characteristic for hexagonal materials in contrast to crystals with rhombohedral symmetry. The m-plane shows the largest sensitivity of e'_5 on the value of C_{14}.

only in the relevant glide planes and are associated with a characteristic Burger's vector **b** that possesses an edge component $\mathbf{b}_\parallel$ in the interface normal to the dislocation line direction allowing strain relaxation in this direction, a screw component $\mathbf{b}_o$ along the dislocation line direction not contributing to strain relaxation, and a tilt component $\mathbf{b}_\perp$ normal to the interface plane not contributing to strain relaxation as well, but causing the lattice tilt. The total tilt and edge components of all Burger's vectors contributing to strain relaxation in a specific direction x determine the lattice tilt in this direction for the partially or fully relaxed layer. The lattice tilt can be calculated via [31]:

$$\theta_T(x_{Al}) = (1-\rho_x)\varepsilon'_{xx}(x_{Al})\frac{|\mathbf{b}_\perp(x_{Al})|}{|\mathbf{b}_\parallel(x_{Al})|}, \qquad (16)$$

where ρ_x is a relaxation parameter in x-direction ($\rho_x = 0$ for a completely relaxed layer, $\rho_x = 1$ for pseudomorphic growth). For the growth on a- and m-plane sapphire, only the pyramidal slip systems can contribute to strain relaxation in c-direction. We chose here the {01.2} r- and {10.1} s-plane slip systems as the ones experimentally observed in α-Al_2O_3 [62–67]. The basal c-glide planes are orthogonal both to the a- as well as m-plane for which the resolved shear stress on the dislocations vanishes. The prismatic a- and m-plane slip systems and associated Burger's vectors can only relieve strain in a direction orthogonal to the c-axis, since the edge component of the Burger's vectors does not have a component along the c-axis direction, since the dislocation line direction is equal to the c-axis.

Further, as special property of the rhombohedral $R\bar{3}c$ crystal symmetry, not all r-planes and s-planes are actual glide planes, since there is a difference between r- and r′-planes [40] as well as s- and s′-planes in the crystal. Only the three (01.2), $(1\bar{1}.2)$ and $(\bar{1}0.2)$ r- as well as the $(0\bar{1}.1)$, $(\bar{1}1.1)$, and (10.1) s-planes are actual crystallographic glide planes within the unit cell in contrast to a hexagonal crystal system [62]. Possible Burger's vectors for the r-planes are $\frac{1}{3}\langle 2\bar{1}.0\rangle$, $\frac{1}{3}\langle 0\bar{1}.1\rangle$ and $\frac{1}{3}\langle \bar{2}0.1\rangle$, while for the s-planes only $\frac{1}{3}\langle \bar{1}2.0\rangle$ and $\frac{1}{3}\langle \bar{1}1.1\rangle$ are allowed [62]. The following discussion for the r-planes holds true for the three s-planes as well, which will not be mentioned explicitly again for the sake of simplicity. The relevant figures would look essentially similar as well for the s-planes with only slight differences in the intersections of the dislocation lines and the position in the unit cell and can be found in Fig. S4 in the supplementary material. Figure 7a and b show the positions of the relevant r-planes and their intersection with the epitaxial (11.0) a- and (10.0) m-planes, respectively. A possible Burger's vector for the $\frac{1}{3}\langle 0\bar{1}.1\rangle$ system for each r-plane is shown as well. As one can see, there is a fundamental difference between the number, inclination and the dislocation line direction for the r-planes to the a-plane or m-plane, respectively. First, only two r-planes can contribute to strain relaxation for the a-growth plane, (01.2) and $(\bar{1}0.2)$. The third r-plane $(1\bar{1}.2)$ is orthogonal to the a-plane and cannot contribute to strain relaxation. For the m-plane, all three r-plane slip systems can contribute to strain relaxation. Second, the adjacent r-planes exhibit different dislocation line orientations. For the a-plane, both adjacent r-planes have the same dislocation line direction, while for the r-planes adjacent to the m-plane, the dislocation lines cross. This can also be seen in Fig.7c and d, where the dislocation lines are shown on the epitaxial planes in a two dimensional depiction. The crossing angles α_r and α_s for the adjacent r- and s-planes, respectively, as defined in Fig. 7d and Fig. S4d are composition-dependent and can be given as:

$$\alpha_r(x_{Al}) = \arctan\left[2\xi(x_{Al})\right] \qquad (17)$$

$$\alpha_s(x_{Al}) = \arctan\left[\xi(x_{Al})\right], \qquad (18)$$

where $\xi(x_{Al}) = \frac{a_F(x_{Al})}{c_F(x_{Al})}$. We further decomposed all possible Burger's vectors lying in the specific r-plane or s-plane into their edge, tilt and screw components in dependence on the Al-content x of the epilayer. The specific decompositions are given in the supplementary material. We found a fundamental difference in the edge and tilt components of the r-plane slip systems for a-plane and m-plane sapphire. When the equivalent Burger's vectors of the adjacent r-planes, e.g. $\frac{1}{3}[0\bar{1}.1]$ for the (01.2) plane and $\frac{1}{3}[10.1]$ for the $(\bar{1}0.2)$ plane, are chosen to have the same sign for the edge component in c-direction for strain relaxation along the c-axis (for opposite sign any equivalent pair of Burger's vectors of the adjacent planes exactly compensate the edge component of each other in c-axis direction), the tilt

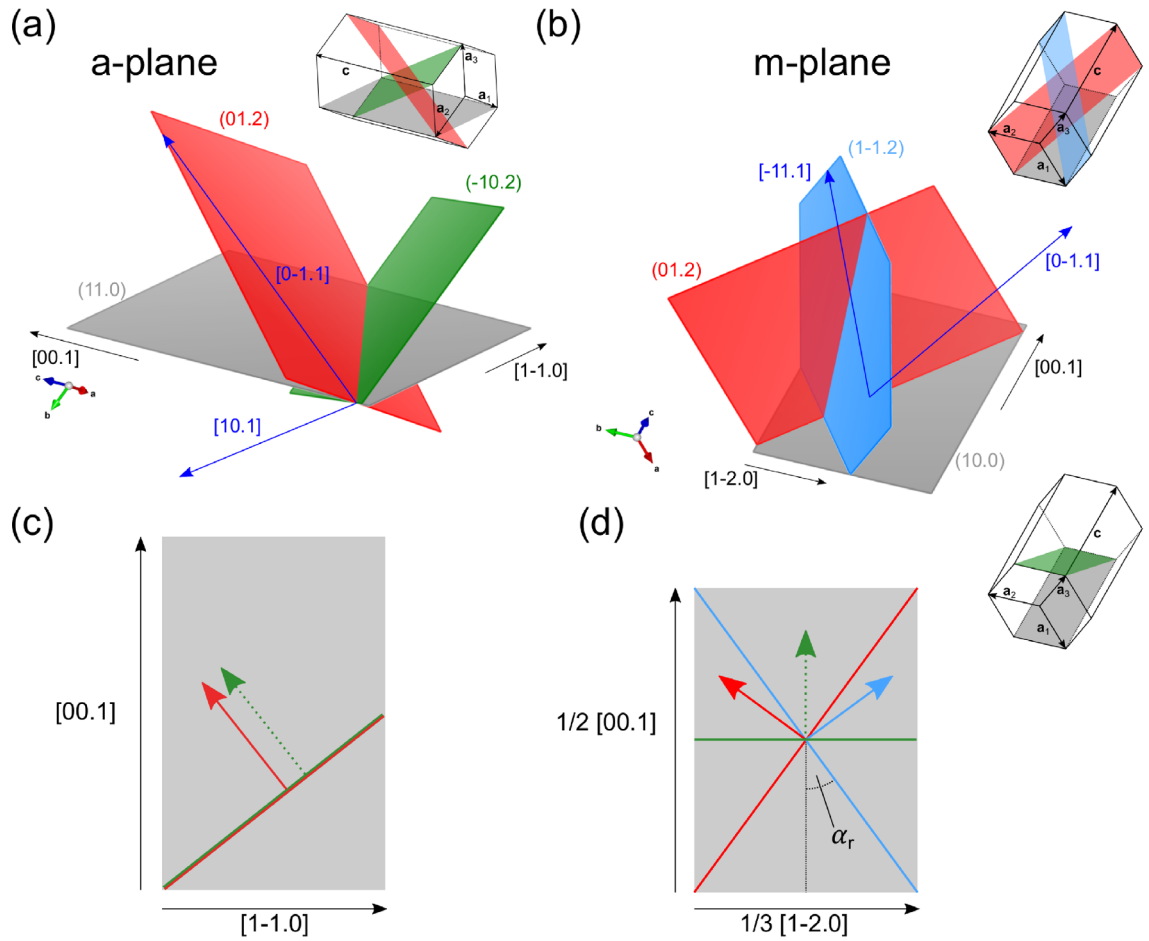

Figure 7: (a) and (b) Schematic depiction of the possible r-plane slip systems and dislocation line directions for (a) samples on a-plane sapphire and (b) on m-plane sapphire. The grey plane is always the epitaxial plane, while the colored planes are the respective adjacent r-glide planes. The third r-plane in (a), the $(1\bar{1}.2)$-plane is perpendicular to the a-plane and cannot contribute to strain relaxation. The third r-plane in (b), the $(\bar{1}0.2)$-plane, contributes to strain relaxation for the m-growth plane, but has been omitted in this depiction for better visibility. Possible $\langle 10.1 \rangle$ Burger's vector directions for the different r-planes are given as well as blue arrows. The smaller hexagons depict the respective orientation of the planes within the hexagonal unit cell. The color code of the planes is the same as in the larger images. For the m-growth plane, also the $(\bar{1}0.2)$-plane is shown in green in the lower hexagon. Images of the planes partially created using VESTA [61]. (c) and (d) Bird's eye view on the (c) a-growth plane and (d) m-growth plane. The colored solid lines are the dislocation line directions within the epitaxial plane for the r-plane slip systems shown in (a) and (b). The same color code applies. The arrows are the corresponding directions of the edge components of the Burger's vectors of the r-plane slip systems. Solid (dashed) arrows indicate upward (downward) tilt component. α_r denotes the crossing angle of the dislocation lines.

components of the Burger's vectors for the a-growth plane will exactly pairwise compensate each other and the tilt vanishes. For the m-growth plane, a triple set of equivalent Burger's vectors (one for each r-plane) with the same sign of the edge component in *c*-axis direction will always have a net tilt component. This is also shown in Fig. 7c and d, where the directions of the edge components of the Burger's vectors are schematically depicted for all possible r-planes.

The consequence of this is that no lattice tilt should be possible for strain relaxation in *c*-axis direction for the growth on a-plane sapphire, while there will always be a lattice tilt in *c*-direction on m-plane sapphire when the r- or s-plane slip systems relieve strain in that direction. This is in perfect agreement with our experimental observations, where a tilt angle is only observed for layers on m-plane sapphire.

For relaxed m-plane InGaN/GaN heterostructures, a global lattice tilt has been observed as well [68, 69]. However, here the lattice is tilted along the *a*-axis direction and two oppositely tilted domains are observed due to prismatic m-plane slip systems that are activated asymmetrically [68].

We note that there is another consequence of the different behavior of the r- and s-plane slip systems on a- and m-growth planes. While the total edge component of a pair of Burger's vectors of these planes exhibits a component in the $[1\bar{1}.0]$ direction for the a-growth plane, i.e. perpendicular to the *c*-axis, the components perpendicular to the *c*-axis for a triple set of equivalent

Burger's vectors in the case of m-plane sapphire compensate each other completely and the total edge component points purely in *c*-axis direction. This means while the r- and s-plane slip systems for layers on a-sapphire can relieve strain both in *c*-axis direction as well as perpendicular to it, the r- and s-plane slip systems for layers on m-sapphire can only relax strain in *c*-axis direction. Strain perpendicular to the *c*-axis can then only be relieved by the prismatic slip systems. An exception might be a symmetry breaking and a preferential activation of only one of the r- or s-plane slip systems adjacent to the epitaxial m-plane. However, then a global lattice tilt in a direction not equal to the *c*-axis would be the consequence.

Numerical modeling of the tilt angle

The tilt angle θ_T as function of x for our layers on m-plane sapphire is shown in Fig. 8a. The tilt angle is only non-vanishing in *c*-axis direction and for the relaxed layers as expected from the discussion above and is increasing with decreasing x due to an increase in lattice mismatch and relieved strain $\varepsilon'_{xx}(x_{Al})$ in agreement with Eq. 16.

To numerically reproduce the lattice tilt, we utilized the decomposition of the Burger's vectors into their components. The possible Burger's vectors for the different r- and s-planes are summarized in Table 2. We included only the Burger's vectors given in red. The $\frac{1}{3}[\bar{1}2.0]$ Burger's vector for the $(\bar{1}0.2)$ and (10.1) plane is purely screw type, while the $\frac{1}{3}[\bar{2}1.0]$ and $\frac{1}{3}[\bar{1}\bar{1}.0]$ Burger's vectors for the (01.2) and $(1\bar{1}.2)$ plane, respectively, exhibit no resolved shear stress for strain in *c*-axis direction as driving force for the movement of the dislocation to relieve strain in this direction. The $\frac{1}{3}[\bar{2}2.\bar{1}]$ and $\frac{1}{3}[0\bar{2}.\bar{1}]$ Burger's vectors for the (01.2) and $(1\bar{1}.2)$ plane, respectively, show a much larger screw component for a lower edge component as the two equivalent $\frac{1}{3}[\bar{2}0.1]$ Burger's vectors with equal length and should therefore contribute little to strain relaxation as the $\frac{1}{3}[\bar{2}0.1]$ Burger's vectors should be preferred. We obtain for the set of Burger's vectors for the three r-planes a total tilt and edge component in dependence on x of:

TABLE 2: The three different r- and s-plane slip systems in rhombohedral α-$(Al_xGa_{1-x})_2O_3$ and the possible Burger's vectors lying in each plane.

plane	Burger's vectors
(01.2)	$\frac{1}{3}[\bar{2}1.0]$ $\frac{1}{3}[0\bar{1}.1]$ $\frac{1}{3}[\bar{2}0.1]$ $\frac{1}{3}[\bar{2}2.\bar{1}]$
$(1\bar{1}.2)$	$\frac{1}{3}[\bar{1}\bar{1}.0]$ $\frac{1}{3}[\bar{1}1.1]$ $\frac{1}{3}[\bar{2}0.1]$ $\frac{1}{3}[0\bar{2}.\bar{1}]$
$(\bar{1}0.2)$	$\frac{1}{3}[\bar{1}2.0]$ $\frac{1}{3}[10.1]$ $\frac{1}{3}[2\bar{2}.1]$ $\frac{1}{3}[02.1]$
$(0\bar{1}.1)$	$\frac{1}{3}[2\bar{1}.1]$ $\frac{1}{3}[10.1]$ $\frac{1}{3}[1\bar{1}.1]$
$(\bar{1}1.1)$	$\frac{1}{3}[11.0]$ $\frac{1}{3}[01.\bar{1}]$ $\frac{1}{3}[10.1]$
(10.1)	$\frac{1}{3}[\bar{1}2.0]$ $\frac{1}{3}[\bar{1}1.1]$ $\frac{1}{3}[0\bar{1}.1]$

The vectors given in red were utilized for the calculation of the tilt angle as explained in the text.

$$\mathbf{b}_{r,\perp}(x_{Al}) = \frac{2}{3}[\bar{1}0.0] \tag{19}$$

$$\mathbf{b}_{r,\parallel}(x_{Al}) = \left(\frac{20\,\xi^2(x_{Al})}{24\,\xi^2(x_{Al})+6}+1\right)[00.1]\,. \tag{20}$$

Considering fully relaxed layers in *c*-axis direction, we obtain for the tilt angle $\theta_T(x_{Al})$:

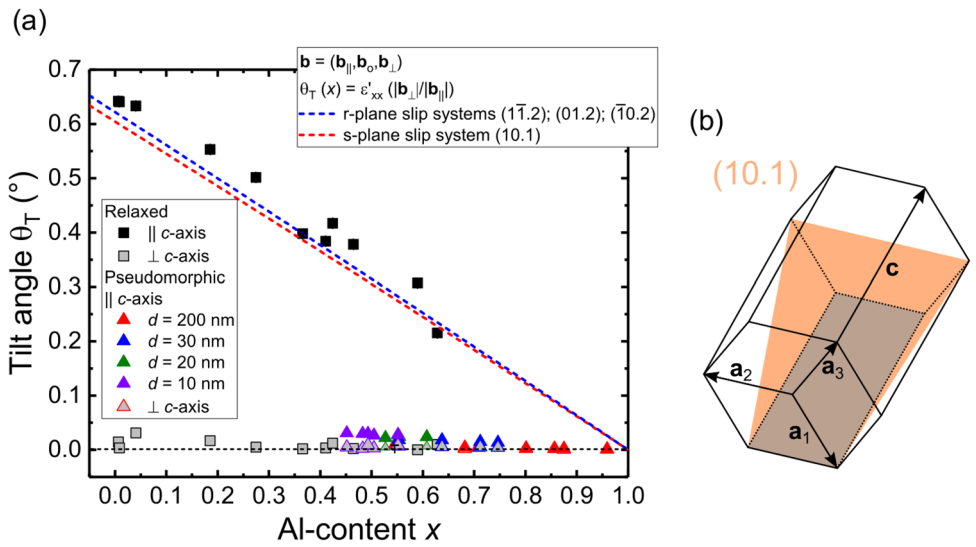

Figure 8: (a) Tilt angle θ_T as function of Al-content x for all α-$(Al_xGa_{1-x})_2O_3$ samples on m-plane sapphire for the *c*-axis within the plane of incidence of the X-ray beam and perpendicular to it. Triangular and quadratic symbols correspond to the determined experimental values. The approximate sample thickness d is color coded as given in the legend. The same color code applies for the completely colored symbols and the symbols with grey filling. The relaxed samples all exhibit a thickness of nominally 200 nm. The blue and red dashed lines are the theoretically expected tilt angles for full strain relaxation due to the r- and s-plane slip systems as given in Eqs. 22 and 24, respectively. (b) Schematic depiction of the relevant (10.1) s-plane for the modeling of the tilt angle shown in orange. The grey plane is the epitaxial m-plane.

$$\theta_{\mathrm{T,r}}(x_{\mathrm{Al}}) = \varepsilon'_{xx}(x_{\mathrm{Al}}) \frac{|\mathbf{b}_{\mathrm{r},\perp}(x_{\mathrm{Al}})|}{|\mathbf{b}_{\mathrm{r},\parallel}(x_{\mathrm{Al}})|} = \frac{2}{3} \frac{\sqrt{3}}{\frac{20\,\xi^2(x_{\mathrm{Al}})}{24\,\xi^2(x_{\mathrm{Al}})+6} + 1} \xi(x_{\mathrm{Al}}) \left(\frac{c_{\mathrm{s}}}{c_{\mathrm{F}}(x_{\mathrm{Al}})} - 1 \right). \quad (21)$$

For the s-planes, we found the (10.1) plane (schematically depicted in Fig. 8b) to be sufficient to explain the tilt angle, for which we obtain for the Burger's vector components:

$$\mathbf{b}_{\mathrm{s},\perp}(x_{\mathrm{Al}}) = \frac{1}{3}[\bar{1}0.0] \quad (22)$$

$$\mathbf{b}_{\mathrm{s},\parallel}(x_{\mathrm{Al}}) = \frac{2}{3}[00.1], \quad (23)$$

and for the tilt angle:

$$\theta_{\mathrm{T,s}}(x_{\mathrm{Al}}) = \frac{\sqrt{3}}{2} \xi(x_{\mathrm{Al}}) \left(\frac{c_{\mathrm{s}}}{c_{\mathrm{F}}(x_{\mathrm{Al}})} - 1 \right). \quad (24)$$

This is reasonable, since the relative portion of the edge component in *c*-axis direction for the s-planes adjacent to the m-plane is considerably lower than for the (10.1) plane or the adjacent r-planes.

The resulting curves are plotted as blue and red dashed curves in Fig. 8a and both reproduce the experimentally observed tilt angles with good agreement. The r-plane or s-plane slip systems should therefore be responsible for the strain relaxation in *c*-axis direction. Considering the larger resolved shear stress for the (10.1) and ($\bar{1}$0.2) planes for strain along the *c*-axis direction compared to the adjacent r- and s-planes, the single s-plane slip system seems to be the more reasonable alternative, since the (10.1) plane should be the first to reach the critical resolved shear stress and get activated. Additionally, defects from s-plane glide have been identified in transmission electron microscopy (TEM) images of strongly relaxed layers on r-plane sapphire [70]. In future studies, the slip lines of samples grown at higher substrate temperatures and close to the critical thickness should be investigated by atomic force microscopy and their crossing angle evaluated to identify the responsible slip systems similar as for samples grown on r-plane sapphire in Refs. [39], [70] and [71]. Alternatively, also TEM investigations could be conducted to reveal the dislocations and dominant Burger's vectors. This was however not in the scope of the present study.

Conclusion

Pseudomorphically strained as well as plastically relaxed α-$(Al_xGa_{1-x})_2O_3$ layers were grown with different thicknesses in the range of 10-200 nm on m- and a-plane sapphire substrates in the full composition range from α-Ga_2O_3 to α-Al_2O_3 by combinatorial PLD [49, 50] utilizing only two elliptically-segmented targets. RSM measurements on the epilayers reveal that pseudomorphic growth is possible for $x_{\mathrm{Al}} \geq 0.45$ for layer thicknesses below 10 nm. For 200 nm layers, the critical Al-content was found to be about $x_{\mathrm{Al}} = 0.8$. The high crystalline quality of the pseudomorphic layers and smooth interfaces were confirmed by the presence of Pendellösung fringes in RSM measurements as well as low broadening of all reflections equal to the broadening of the substrate reflections. A fundamental difference in the behavior of α-$(Al_xGa_{1-x})_2O_3$ layers on epitaxial m- and a-growth planes has been identified. The pseudomorphic α-$(Al_xGa_{1-x})_2O_3$ thin films on m-plane sapphire show a pronounced lattice shear in *c*-axis direction not present for layers on a-plane sapphire. Similarly, relaxed layers on m-plane sapphire exhibit a strong lattice tilt in *c*-axis direction that is not present on a-plane sapphire as well. The in- and out-of-plane lattice constants of all layers were evaluated and the relaxed layers follow a linear trend as expected from Vegard's law with a slight residual in-plane strain perpendicular to the *c*-axis. The out-of-plane lattice constants as well as the shear strains as function of *x* were modeled using our continuum elasticity theory for rhombohedral heterostructures [31, 45, 46]. A good agreement between theoretical values and the experimental data was found corroborating the theoretically calculated entries of the elastic stiffness tensor for α-Ga_2O_3 and the experimentally determined values for α-Al_2O_3. Especially the validity of the C_{14} component could be confirmed and the m-plane was identified as most suitable epitaxial plane for its determination. The possible slip systems for strain relaxation for the epitaxial m- and a-planes were examined and also here a fundamental difference was found explaining the occurence of the lattice tilt only for relaxed m-plane epilayers. The tilt angle as a function of *x* was reproduced utilizing edge and tilt components of relevant Burger's vectors and the pyramidal r- or s-plane slip systems were identified as possibly responsible for plastic strain relaxation in *c*-axis direction for layers beyond the critical thickness. These findings should find potential use in the further design, growth and understanding of α-$(Al_xGa_{1-x})_2O_3$ based heterostructures for power device applications.

Materials and methods

The α-$(Al_xGa_{1-x})_2O_3$ thin films with nominal thicknesses of about 10, 20, 30 and 200 nm were grown by PLD using either $5 \times 5\,\mathrm{mm}^2$ or $10 \times 10\,\mathrm{mm}^2$ m- as well as a-plane sapphire substrates (Crystec). For the films with 30 nm and 200 nm thickness, four $5 \times 5\,\mathrm{mm}^2$ pieces including one m- and one a-plane sapphire cut were placed in a four-piece sample holder to ensure identical process parameters for the layers on the different growth planes. The 10 nm and 20 nm samples were grown on single $10 \times 10\,\mathrm{mm}^2$ m-plane sapphire substrates to

increase the intensity in XRD measurements. We employed a 248 nm KrF excimer laser at a pulse energy of 650 mJ to ablate the targets. The laser was focused on the target surface to an area of $2 \times 6.5\,mm^2$ corresponding to a laser fluence of $2.6\,J\,cm^{-2}$. 10 Hz was chosen as repetition frequency for all samples. A detailed description of the PLD setup can be found in Refs. [72] and [73]. The oxygen partial pressure was chosen as $p(O_2) = 6 \times 10^{-4}$ mbar and the growth temperature was set to $T_g \approx 720°C$ for all layers. The Al-content in the layers was controllably varied in this study by employing elliptically-segmented targets. We used only two targets in total, a $Ga_2O_3/(Al_{0.4}Ga_{0.6})_2O_3$ and a $(Al_{0.4}Ga_{0.6})_2O_3/Al_2O_3$ target (inner segment/outer segment).

Employing elliptically-segmented targets in combination with a rotation of the target and a fixed radial position r of the laser spot on the target surface enables direct and reproducible control over the thin film stoichiometry which is a function of r (vertical continuous composition spread (VCCS) or also DCS PLD technique) as described in detail in Refs. [49] and [50]. The Al_2O_3 (99.997 % purity, Alfa Aesar) and Ga_2O_3 (99.999 % purity, Alfa Aesar) target powders in the respective mixtures were ball-milled, cold-pressed and sintered in air at a temperature of 1550°C for 72 h.

XRD 2θ-ω scans and reciprocal space map measurements (RSMs) were performed employing a PANalytical X'pert PRO MRD diffractometer with Cu K_α radiation using a parabolic mirror and PIXcel^{3D} detector. In total, 2 symmetric and 4 asymmetric reflections were measured per sample employing the frame-based option of the PIXcel^{3D} detector that allows a reduction of the measurement time by a factor of 5 in comparison to conventionally recorded RSMs.

The Al-content of the 200 nm samples was determined by energy dispersive X-ray spectroscopy (EDX) utilizing Nova NanoLab 200 by FEI company. Due to the low thickness of the other layers and the probable overestimation of the Al-content due to the substrate signal in EDX measurements, X-ray photoelectron spectroscopy (XPS) measurements were utilized to determine the Al-content of the 10, 20 and 30 nm layers. XPS measurements were performed with a JEOL JPS-9030 system and a Mg K_α X-ray source for excitation. The relative sensitivity factors were calibrated by measuring binary Al_2O_3 and Ga_2O_3 reference samples and assuming perfect stoichiometry. The film thicknesses were either determined by spectroscopic ellipsometry or estimated from the positions of Pendellösung fringes in RSM measurements. The exact film thicknesses for the samples with nominal 200 nm thickness grown with 10000 PLD pulses show a slight variation with Al-content x. The thickness values for the samples on m-plane sapphire can be found in Fig. S5 in the supplementary material, where also the film thicknesses for selected samples with nominal 10, 20 and 30 nm thickness determined by spectroscopic ellipsometry as well as estimated by the separation of Pendellösung fringes are displayed for comparison.

Acknowledgments

We are indebted to Monika Hahn for PLD target fabrication and Holger Hochmuth for the implementation of VCCS PLD in the PLD setup. We further thank Chris Sturm for film thickness determination by spectroscopic ellipsometry and Eduard Rose for the creation of a program code to display RSMs. We are also grateful to Ingvild Thue Jensen (SINTEF Materials Physics, Oslo) and Ylva K. Hommedal (University of Oslo, Semiconductor Physics) for additional XPS measurements to determine the composition of the 30 nm thick layers on a-plane sapphire.

Funding

This work was supported by the European Social Fund within the Young Investigator Group "Oxide Heterostructures" (SAB 100310460), by Universität Leipzig in research profile area "Complex Matter" as well as within the framework of GraFOx, a Leibniz-Science Campus partially funded by the Leibniz Association. M.K. also acknowledges the Leipzig School for Natural Sciences BuildMoNa. Open Access funding enabled and organized by Projekt DEAL.

Data availability

The data that support the findings of this study are available within the article and its supplementary material or are available from the corresponding author upon reasonable request.

Declarations

Conflict of interest On behalf of all authors, the corresponding author states that there is no conflict of interest.

Supplementray Information

The online version contains supplementary material available at https://doi.org/10.1557/s43578-021-00375-3.

Open Access

References

1. M. Higashiwaki, K. Sasaki, H. Murakami, Y. Kumagai, A. Koukitu, A. Kuramata, T. Masui, S. Yamakoshi, Recent progress in Ga_2O_3 power devices. Semicond. Sci. Technol. **31**(3), 034001 (2016). https://doi.org/10.1088/0268-1242/31/3/034001
2. Y. Zhang, C. Joishi, Z. Xia, M. Brenner, S. Lodha, S. Rajan, Demonstration of β-$(Al_xGa_{1-x})_2O_3/Ga_2O_3$ double heterostructure field effect transistors. Appl. Phys. Lett. **112**(23), 233503 (2018). https://doi.org/10.1063/1.5037095
3. Y. Zhang, A. Neal, Z. Xia, C. Joishi, J.M. Johnson, Y. Zheng, S. Bajaj, M. Brenner, D. Dorsey, K. Chabak, G. Jessen, J. Hwang, S. Mou, J.P. Heremans, S. Rajan, Demonstration of high mobility and quantum transport in modulation-doped β-$(Al_xGa_{1-x})_2O_3$/Ga_2O heterostructures. Appl. Phys. Lett. **112**(17), 173502 (2018). https://doi.org/10.1063/1.5025704
4. Y. Zhang, Z. Xia, J. Mcglone, W. Sun, C. Joishi, A.R. Arehart, S.A. Ringel, S. Rajan, Evaluation of low-temperature saturation velocity in β-$(Al_xGa_{1-x})_2O_3/Ga_2O_3$ modulation-doped field-effect transistors. IEEE Trans. Electron Dev. **66**(3), 1574 (2019). https://doi.org/10.1109/TED.2018.2889573
5. H. von Wenckstern, Group-III sesquioxides growth, physical properties and devices. Adv. Electron. Mater. **3**(9), 1600350 (2017). https://doi.org/10.1002/aelm.201600350
6. S.J. Pearton, J. Yang, P.H. Cary, F. Ren, J. Kim, M.J. Tadjer, M.A. Mastro, A review of Ga_2O_3 materials, processing, and devices. Appl. Phys. Rev. **5**(1), 011301 (2018). https://doi.org/10.1063/1.5006941
7. J. Zhang, J. Shi, D.C. Qi, L. Chen, K.H.L. Zhang, Recent progress on the electronic structure, defect, and doping properties of Ga_2O_3. APL Mater. **8**(2), 020906 (2020). https://doi.org/10.1063/1.5142999
8. A. Hassa, M. Grundmann, H. von Wenckstern, Progression of group-III sesquioxides epitaxy, solubility and desorption. J. Phys. D **54**(22), 223001 (2021). https://doi.org/10.1088/1361-6463/abd4a4
9. D. Shinohara, S. Fujita, Heteroepitaxy of corundum-structured α-Ga_2O_3 thin films on α-Al_2O_3 substrates by ultrasonic mist chemical vapor deposition. Jpn. J. Appl. Phys. **47**(9), 7311 (2008). https://doi.org/10.1143/JJAP.47.7311
10. S. Fujita, K. Kaneko, Epitaxial growth of corundum-structured wide band gap III-oxide semiconductor thin films. J. Cryst. Growth **401**, 588 (2014). https://doi.org/10.1016/j.jcrysgro.2014.02.032
11. K. Kaneko, S. Fujita, T. Hitora, A power device material of corundum-structured Ga_2O_3 fabricated by MIST EPITAXY® technique. Jpn. J. Appl. Phys. **57**(22), 02CB18 (2018). https://doi.org/10.7567/JJAP.57.02CB18
12. M. Kracht, A. Karg, J. Schörmann, M. Weinhold, D. Zink, F. Michel, M. Rohnke, M. Schowalter, B. Gerken, A. Rosenauer, P.J. Klar, J. Janek, M. Eickhoff, Tin-assisted synthesis of ε-Ga_2O_3 by molecular beam epitaxy. Phys. Rev. Appl. **8**(5), 054002 (2017). https://doi.org/10.1103/PhysRevApplied.8.054002
13. M. Kneiß, A. Hassa, D. Splith, C. Sturm, H. von Wenckstern, T. Schultz, N. Koch, M. Lorenz, M. Grundmann, Tin-assisted heteroepitaxial PLD-growth of κ-Ga_2O_3 thin films with high crystalline quality. APL Mater. **7**(2), 022516 (2019). https://doi.org/10.1063/1.5054378
14. V. Gottschalch, S. Merker, S. Blaurock, M. Kneiß, U. Teschner, M. Grundmann, H. Krautscheid, Heteroepitaxial growth of α-, β-, γ- and κ-Ga_2O_3 phases by metalorganic vapor phase epitaxy. J. Cryst. Growth **510**, 76 (2019). https://doi.org/10.1016/j.jcrysgro.2019.01.018
15. T. Oshima, Y. Kato, E. Magome, E. Kobayashi, K. Takahashi, Characterization of pseudomorphic γ-Ga_2O_3 and γ-Al_2O_3 films on $MgAl_2O_4$ substrates and the bandalignment at the coherent γ-Ga_2O_3/Al_2O_3 heterojunction interface. Jpn. J. Appl. Phys. **58**(6), 060910 (2019). https://doi.org/10.7567/1347-4065/ab219f
16. Y. Kato, M. Imura, Y. Nakayama, M. Takeguchi, T. Oshima, Fabrication of coherent γ-Al_2O_3/Ga_2O_3 superlattices on $MgAl_2O_4$ substrates. Appl. Phys. Express **12**(6), 065503 (2019). https://doi.org/10.7567/1882-0786/ab2196
17. M. Oda, K. Kaneko, S. Fujita, T. Hitora, Crack-free thick (≈5 μm) α-Ga_2O_3 films on sapphire substrates with α-$(Al,Ga)_2O_3$ buffer layers. Jpn. J. Appl. Phys. **55**(12), 1202B4 (2016). https://doi.org/10.7567/JJAP.55.1202B4
18. D.W. Jeon, H. Son, J. Hwang, A.Y. Polyakov, N.B. Smirnov, I.V. Shchemerov, A.V. Chernykh, A.I. Kochkova, S.J. Pearton, I.H. Lee, Electrical properties, structural properties, and deep trap spectra of thin α-Ga_2O_3 films grown by halide vapor phase epitaxy on basal plane sapphire substrates. APL Mater. **6**(12), 121110 (2018). https://doi.org/10.1063/1.5075718
19. A.I. Pechnikov, S.I. Stepanov, A.V. Chikiryaka, M.P. Scheglov, M.A. Odnobludov, V.I. Nikolaev, Thick α-Ga_2O_3 layers on sapphire substrates grown by halide epitaxy. Semiconductors **53**(6), 780 (2019). https://doi.org/10.1134/S1063782619060150
20. T. Ma, X. Chen, F. Ren, S. Zhu, S. Gu, R. Zhang, Y. Zheng, J. Ye, Heteroepitaxial growth of thick α-Ga_2O_3 film on sapphire (0001) by MIST-CVD technique. J. Semicond. **40**(1), 012804 (2019). https://doi.org/10.1088/1674-4926/40/1/012804
21. K. Kawara, Y. Oshima, M. Okigawa, T. Shinohe, Elimination of threading dislocations in α-Ga_2O_3 by double-layered epitaxial lateral overgrowth. Appl. Phys. Express **13**(7), 075507 (2020). https://doi.org/10.35848/1882-0786/ab9fc5
22. S. Fujita, M. Oda, K. Kaneko, T. Hitora, Evolution of corundum-structured III-oxide semiconductors growth, properties, and

devices. Jpn. J. Appl. Phys. **55**(12), 1202A3 (2016). https://doi.org/10.7567/JJAP.55.1202A3

23. T. Uchida, K. Kaneko, S. Fujita, Electrical characterization of Si-doped n-type α-Ga_2O_3 on sapphire substrates. MRS Adv. **3**(3), 171 (2018). https://doi.org/10.1557/adv.2018.45
24. K. Akaiwa, K. Kaneko, K. Ichino, S. Fujita, Conductivity control of Sn-doped α-Ga_2O_3 thin films grown on sapphire substrates. Jpn. J. Appl. Phys. **55**(12), 1202BA (2016). https://doi.org/10.7567/JJAP.55.1202BA
25. S. Morimoto, H. Nishinaka, M. Yoshimoto, Growth and characterization of F-doped α-Ga_2O_3 thin films with low electrical resistivity. Thin Solid Films **682**, 18 (2019). https://doi.org/10.1016/j.tsf.2019.04.051
26. K. Akaiwa, K. Ota, T. Sekiyama, T. Abe, T. Shinohe, K. Ichino, Electrical properties of Sn-doped α-Ga_2O_3 films on m-plane sapphire substrates grown by mist chemical vapor deposition. Phys. Status Solidi A **217**(3), 1900632 (2020). https://doi.org/10.1002/pssa.201900632
27. R. Kumaran, T. Tiedje, S.E. Webster, S. Penson, W. Li, Epitaxial Nd-doped α-$(Al_xGa_{1-x})_2O_3$ films on sapphire for solid-state waveguide lasers. Opt. Lett. **35**(22), 3793 (2010). https://doi.org/10.1364/OL.35.003793
28. H. Ito, K. Kaneko, S. Fujita, Growth and band gap control of corundum-structured α-$(AlGa)_2O_3$ thin films on sapphire by spray-assisted mist chemical vapor deposition. Jpn. J. Appl. Phys. **51**(10R), 100207 (2012). https://doi.org/10.1143/JJAP.51.100207
29. K. Kaneko, K. Suzuki, Y. Ito, S. Fujita, Growth characteristics of corundum-structured α-$(Al_xGa_{1-x})_2O_3/Ga_2O_3$ heterostructures on sapphire substrates. J. Cryst. Growth **436**, 150 (2016). https://doi.org/10.1016/j.jcrysgro.2015.12.013
30. G.T. Dang, T. Yasuoka, Y. Tagashira, T. Tadokoro, W. Theiss, T. Kawaharamura, Bandgap engineering of α-$(Al_xGa_{1-x})_2O_3$ by a mist chemical vapor deposition two-chamber system and verification of Vegard's Law. Appl. Phys. Lett. **113**(6), 062102 (2018). https://doi.org/10.1063/1.5037678
31. M. Grundmann, M. Lorenz, Anisotropic strain relaxation through prismatic and basal slip in α-$(Al,Ga)_2O_3$ on R-plane Al_2O_3. APL Mater. **8**(2), 021108 (2020). https://doi.org/10.1063/1.5144744
32. A. Hassa, P. Storm, M. Kneiß, D. Splith, H. von Wenckstern, M. Lorenz, M. Grundmann, Structural and elastic properties of α-$(Al_xGa_{1-x})_2O_3$ thin films on (11.0) Al_2O_3 substrates for the entire composition range. Phys. Status Solidi B **258**(2), 2000394 (2021). https://doi.org/10.1002/pssb.202000394
33. R. Jinno, C.S. Chang, T. Onuma, Y. Cho, S.T. Ho, D. Rowe, M.C. Cao, K. Lee, V. Protasenko, D.G. Schlom, D.A. Muller, H.G. Xing, D. Jena, Crystal orientation dictated epitaxy of ultrawide-bandgap 5.4- to 8.6-eV α-$(Al,Ga)_2O_3$ on m-plane sapphire. Sci. Adv. **7**(2), eabd5891 (2021). https://doi.org/10.1126/sciadv.abd5891
34. R. Jinno, T. Uchida, K. Kaneko, S. Fujita, Reduction in edge dislocation density in corundum-structured α-Ga_2O_3 layers on sapphire substrates with quasi-graded α-$(Al,Ga)_2O_3$ buffer layers. Appl. Phys. Express **9**(7), 071101 (2016). https://doi.org/10.7567/APEX.9.071101
35. T.C. Ma, X.H. Chen, Y. Kuang, L. Li, J. Li, F. Kremer, F.F. Ren, S.L. Gu, R. Zhang, Y.D. Zheng, H.H. Tan, C. Jagadish, J.D. Ye, On the origin of dislocation generation and annihilation in α-Ga_2O_3 epilayers on sapphire. Appl. Phys. Lett. **115**(18), 182101 (2019). https://doi.org/10.1063/1.5120554
36. M. Lorenz, S. Hohenberger, E. Rose, M. Grundmann, Atomically stepped, pseudomorphic, corundum-phase $(Al_xGa_{1-x})_2O_3$ thin films ($0 \le x < 0.08$) grown on R-plane sapphire. Appl. Phys. Lett. **113**(23), 231902 (2018). https://doi.org/10.1063/1.5059374
37. T. Oshima, Y. Kato, M. Imura, Y. Nakayama, M. Takeguchi, α-Al_2O_3/Ga_2O_3 superlattices coherently grown on r-plane sapphire. Appl. Phys. Express **11**(6), 065501 (2018). https://doi.org/10.7567/APEX.11.065501
38. M. Kracht, A. Karg, M. Feneberg, J. Bläsing, J. Schörmann, R. Goldhahn, M. Eickhoff, Anisotropic optical properties of metastable $(01\bar{1}2)$ α-Ga_2O_3 grown by plasma-assisted molecular beam epitaxy. Phys. Rev. Appl. **10**(2), 024047 (2018). https://doi.org/10.1103/PhysRevApplied.10.024047
39. M. Grundmann, T. Stralka, M. Lorenz, Epitaxial growth and strain relaxation of corundum-phase $(Al,Ga)_2O_3$ thin films from pulsed laser deposition at 1000°C on r-plane Al_2O_3. Appl. Phys. Lett. **117**(24), 242102 (2020). https://doi.org/10.1063/5.0030675
40. M. Grundmann, M. Lorenz, Azimuthal anisotropy of rhombohedral (corundum-phase) heterostructures. Phys. Status Solidi B **258**(7), 2100104 (2021). https://doi.org/10.1002/pssb.202100104
41. Z. Cheng, M. Hanke, P. Vogt, O. Bierwagen, A. Trampert, Phase formation and strain relaxation of Ga_2O_3 on c-plane and a-plane sapphire substrates as studied by synchrotron-based x-ray diffraction. Appl. Phys. Lett. **111**(16), 162104 (2017). https://doi.org/10.1063/1.4998804
42. R. Jinno, N. Yoshimura, K. Kaneko, S. Fujita, Enhancement of epitaxial lateral overgrowth in the mist chemical vapor deposition of α-Ga_2O_3 by using a-plane sapphire substrate. Jpn. J. Appl. Phys. **58**(12), 120912 (2019). https://doi.org/10.7567/1347-4065/ab55c6
43. D. Guo, X. Zhao, Y. Zhi, W. Cui, Y. Huang, Y. An, P. Li, Z. Wu, W. Tang, Epitaxial growth and solar-blind photoelectric properties of corundum-structured α-Ga_2O_3 thin films. Mater. Lett. **164**, 364 (2016). https://doi.org/10.1016/j.matlet.2015.11.001
44. T. Maeda, M. Okigawa, Y. Kato, I. Takahashi, T. Shinohe, Defect-insensitive current–voltage characteristics of Schottky barrier diode formed on heteroepitaxial α-Ga_2O_3 grown by mist chemical vapor deposition. AIP Adv. **10**(12), 125119 (2020). https://doi.org/10.1063/5.0028985
45. M. Grundmann, Elastic theory of pseudomorphic monoclinic and rhombohedral heterostructures. J. Appl. Phys. **124**(18), 185302 (2018). https://doi.org/10.1063/1.5045845

46. M. Grundmann, A most general and facile recipe for the calculation of heteroepitaxial strain. Phys. Status Solidi B **257**(12), 2000323 (2020). https://doi.org/10.1002/pssb.202000323
47. J. Furthmüller, F. Bechstedt, Quasiparticle bands and spectra of Ga_2O_3 polymorphs. Phys. Rev. B **93**(11), 115204 (2016). https://doi.org/10.1103/PhysRevB.93.115204
48. M. Grundmann, J. Zúniga-Pérez, Pseudomorphic ZnO-based heterostructures from polar through all semipolar to nonpolar orientations. Phys. Status Solidi B **253**(2), 351 (2016). https://doi.org/10.1002/pssb.201552535
49. M. Kneiß, P. Storm, G. Benndorf, M. Grundmann, H. Von Wenckstern, Combinatorial material science and strain engineering enabled by pulsed laser deposition using radially segmented targets. ACS Comb. Sci. **20**(11), 643 (2018). https://doi.org/10.1021/acscombsci.8b00100
50. H. von Wenckstern, M. Kneiß, A. Hassa, P. Storm, D. Splith, M. Grundmann, A review of the segmented-target approach to combinatorial material synthesis by pulsed-laser deposition. Phys. Status Solidi B **257**(7), 1900626 (2020). https://doi.org/10.1002/pssb.201900626
51. M. Li, C.R. Becker, R. Gall, W. Faschinger, G. Landwehr, X-ray reciprocal space mapping of a (112) oriented HgTe/$Hg_{0.1}Cd_{0.9}Te$ superlattice. Appl. Phys. Lett. **71**(13), 1822 (1997). https://doi.org/10.1063/1.119410
52. R.H. Sewell, C.A. Musca, J.M. Dell, L. Faraone, B.F. Usher, T. Dieing, High-resolution X-ray diffraction studies of molecular beam epitaxy-grown HgCdTe heterostructures and CdZnTe substrates. J. Electron. Mater. **34**(6), 795 (2005). https://doi.org/10.1007/s11664-005-0023-7
53. M. Polat, O. Ari, O. Öztürk, Y. Selamet, Reciprocal space mapping study of CdTe epilayer grown by molecular beam epitaxy on (2 1 1)B GaAs substrate. Mater. Res. Express **4**(3), 035904 (2017). https://doi.org/10.1088/2053-1591/aa61b8
54. R. Schewski, G. Wagner, M. Baldini, D. Gogova, Z. Galazka, T. Schulz, T. Remmele, T. Markurt, H. von Wenckstern, M. Grundmann, O. Bierwagen, P. Vogt, M. Albrecht, Epitaxial stabilization of pseudomorphic α-Ga_2O_3 on sapphire (0001). Appl. Phys. Express **8**(1), 011101 (2015). https://doi.org/10.7567/APEX.8.011101
55. W.J. Campbell, C. Grain, Thermal expansion of alpha-alumina. Adv. X-ray Anal. **5**, 244 (1961). https://doi.org/10.1154/s0376030800001609
56. L.J. Eckert, R.C. Bradt, Thermal expansion of alpha Ga_2O_3. J. Am. Ceram. Soc. **56**(4), 229 (1973). https://doi.org/10.1111/j.1151-2916.1973.tb12471.x
57. W.M. Yim, R.J. Paff, Thermal expansion of AlN, sapphire, and silicon. J. Appl. Phys. **45**(3), 1456 (1974). https://doi.org/10.1063/1.1663432
58. D.B. Hovis, A. Reddy, A.H. Heuer, X-ray elastic constants for α-Al_2O_3. Appl. Phys. Lett. **88**(13), 131910 (2006). https://doi.org/10.1063/1.2189071
59. V. Pishchik, L.A. Lytvynov, E.R. Dobrovinskaya, *Sapphire: Material, Manufacturing, Applications* (Springer, Boston, 2009). https://doi.org/10.1007/978-0-387-85695-7
60. M. Marezio, J.P. Remeika, Bond lengths in the α-Ga_2O_3 structure and the high-pressure phase of $Ga_{2-x}Fe_xO_3$. J. Chem. Phys. **46**(5), 1862 (1967). https://doi.org/10.1063/1.1840945
61. K. Momma, F. Izumi, VESTA 3 for three-dimensional visualization of crystal, volumetric and morphology data. J. Appl. Crystallogr. **44**(6), 1272 (2011). https://doi.org/10.1107/S0021889811038970
62. J.D. Snow, A.H. Heuer, Slip systems in Al_2O_3. J. Am. Ceram. Soc. **56**(3), 153 (1973). https://doi.org/10.1111/j.1151-2916.1973.tb15432.x
63. J. Cadoz, B. Pellissier, Influence of three-fold symmetry on pyramidal slip of alumina single crystal. Scr. Metall. **10**(7), 597 (1976). https://doi.org/10.1016/0036-9748(76)90185-X
64. R.E. Tressler, D.J. Barber, Yielding and flow of c-axis sapphire filaments. J. Am. Ceram. Soc. **57**(1), 13 (1974). https://doi.org/10.1111/j.1151-2916.1974.tb11353.x
65. B.J. Hockey, Plastic deformation of aluminum oxide by indentation and abrasion. J. Am. Ceram. Soc. **54**(5), 223 (1971). https://doi.org/10.1111/j.1151-2916.1971.tb12277.x
66. D.J. Gooch, G.W. Groves, The creep of sapphire filament with orientations close to the c-axis. J. Mater. Sci. **8**(9), 1238 (1973). https://doi.org/10.1007/BF00549338
67. P.D. Bayer, R.E. Cooper, A new slip system in sapphire. J. Mater. Sci. **2**(3), 301 (1967). https://doi.org/10.1007/BF00555392
68. S. Yoshida, T. Yokogawa, Y. Imai, S. Kimura, O. Sakata, Evidence of lattice tilt and slip in m-plane InGaN/GaN heterostructure. Appl. Phys. Lett. **99**(13), 131909 (2011). https://doi.org/10.1063/1.3644978
69. K. Shojiki, T. Hanada, T. Shimada, Y. Liu, R. Katayama, T. Matsuoka, Tilted domain and indium content of InGaN layer on m-plane GaN substrate grown by metalorganic vapor phase epitaxy. Jpn. J. Appl. Phys. **51**, 04DH01 (2012). https://doi.org/10.1143/JJAP.51.04DH01
70. M. Grundmann, T. Stralka, M. Lorenz, S. Selle, C. Patzig, T. Höche, Plastic strain relaxation and alloy instability in epitaxial corundum-phase $(Al,Ga)_2O_3$ thin films on r-plane Al_2O_3. Mater. Adv. **2**(13), 4316 (2021). https://doi.org/10.1039/D1MA00204J
71. M. Grundmann, Universal relation for the orientation of dislocations from prismatic slip systems in hexagonal and rhombohedral strained heterostructures. Appl. Phys. Lett. **116**(8), 082104 (2020). https://doi.org/10.1063/1.5140977
72. M. Lorenz, in *Transparent Conduct. Zinc Oxide*. ed. by K. Ellmer, A. Klein, B. Rech (Springer, Berlin, 2008), pp. 303–357. https://doi.org/10.1007/978-3-540-73612-7_7
73. M. Lorenz, *Digital Encyclopedia of Applied Physics (Chap. Eap810)* (Wiley, Weinheim, 2019), pp. 1–29. https://doi.org/10.1002/3527600434.eap810